Supporting Information

Dejana Pejak Simunec, Michael Breedon, Faizan U.R. Muhammad, Louis Kyratzis, Antonella Sola*

Commonwealth Scientific and Industrial Research Organisation (CSIRO), Manufacturing Business Unit

Research Way, Melbourne VIC, 3168, Australia

**Corresponding author,* Dejana.pejak@csiro.au

Appendix A - PCB design

The PCB board was designed to the aim of measuring the FFF sensors' response taking into account the anisotropy caused by extruding and printing. The PCB board was milled to copper traces as per Figure A.1b.

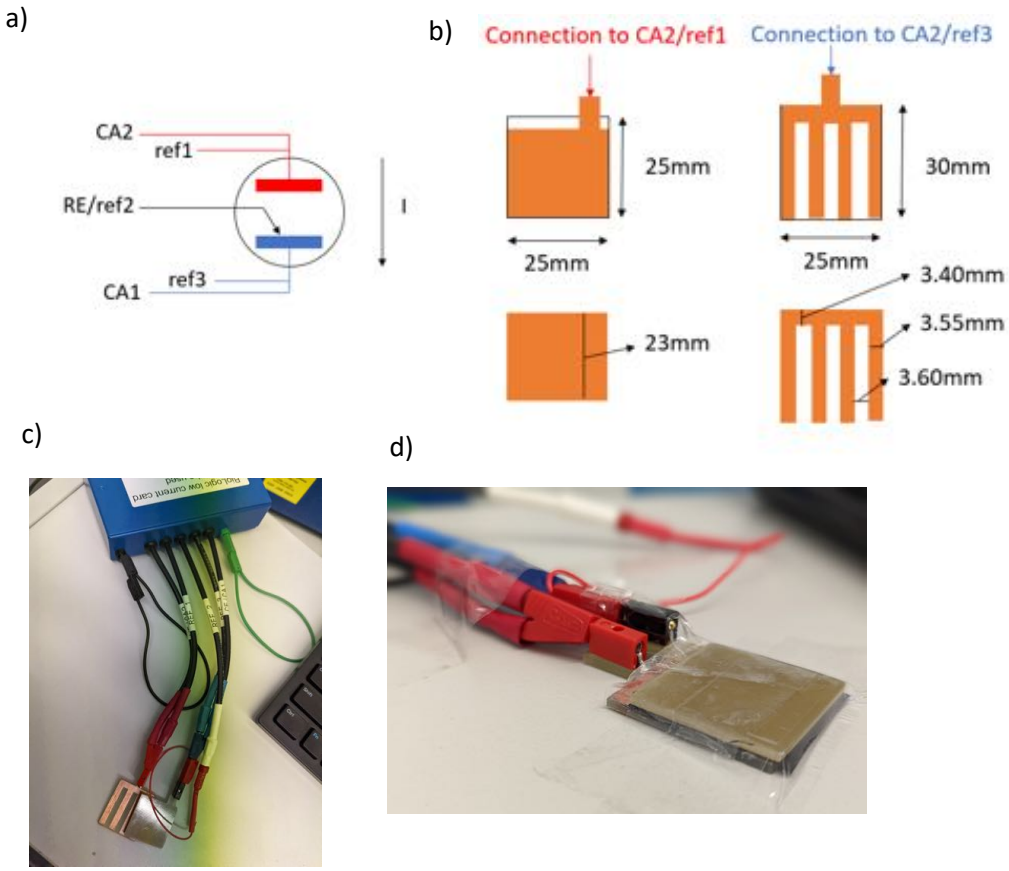

FigureA.1 a) circuit diagram for PCB connection to potentiometer, b) schematic showing the dimensions of the copper traces of the PCB board, c) photograph showing the actual connection with the potentiometer low-current module, d) PCB board fixed to the benchtop with the wire connections secured with tape.

Appendix B – Effect of scan rate on CV curves of TPU/CB (EEL) sensors

The effect of the scan rate on the CV curves is shown for TPU/CB (EEL) sensors in Figure B.1. Only TPU/CB (EEL) was evaluated with varying scan rates to establish a baseline as the main conductive component. Varying the scan rate in CV curves may reveal inconsistencies in an otherwise linear behaviour which are generally observed at low scan rates (i.e., 5mV/s). At a scan rate of 20mV/s, the CV curves remained smooth, registering an observable hysteresis, while the scan time was reduced by 4 hours. Increasing the scan rates at 100 and 1000mV/s produced smooth CV curves as well, but the hysteresis was less significant as the material does not rapidly respond to applied potential. Therefore, in order to capture hysteresis behaviour as well as decreasing the time taken to capture the data, a scan rate of 20mV/s was chosen to conduct CV scans on all sensors (discussed in the main text with regard to Figure 5).

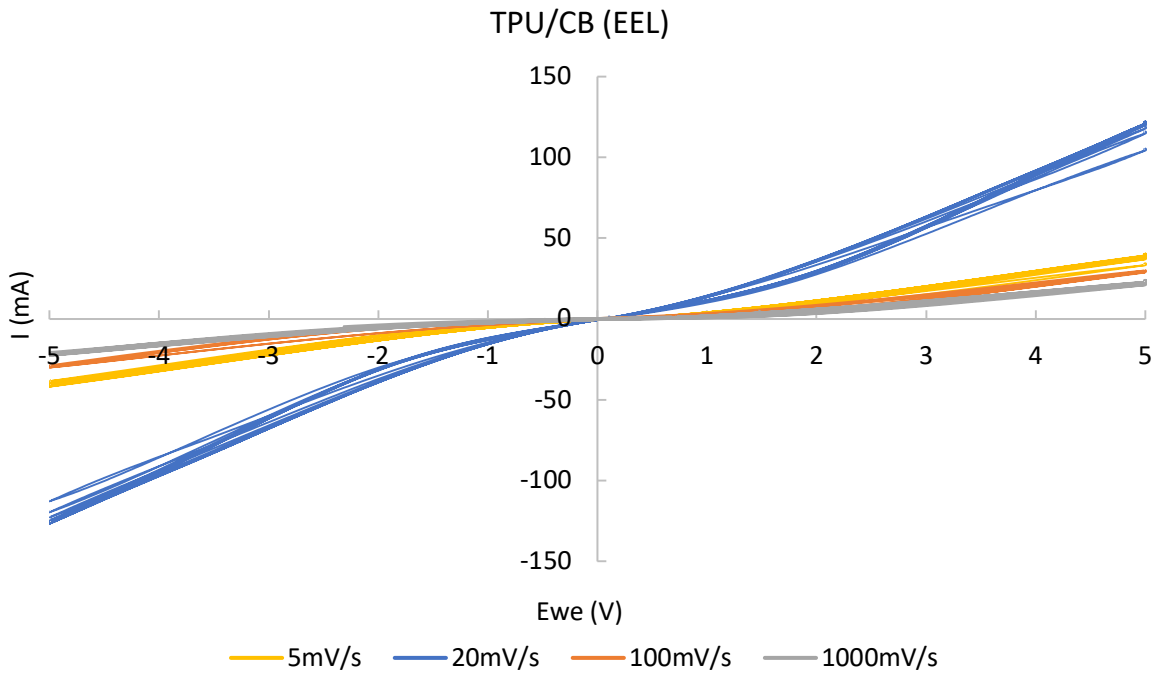

Figure B.1 CV curves with varied scan rates (5, 20, 100 and 1000mV/s) for TPU/CB (EEL) sensors for consecutive 10 cycles.

Appendix C - Chronoamperometry scans using constant force

To assess the electrical response elicited by a constant impact force, steel tubes with an external diameter of 6.35 mm were cut into 20, 30 and 40 cm lengths and dropped from a height of 20 mm in the centre of the PCB board, to determine material response to three different, highly repeatable impact forces. The sensors were mounted in the PCB board and held between the electrodes with clear tape. The board was secured onto the bench and the pipes were dropped over it using a polyvinyl chloride (PVC) cylinder mounted 20 mm above the PCB board with a milled hole at the top to allow the steel tube to drop smoothly through (see Figure C.1a). Additionally, to prevent friction between the mounted tube and the steel pipes, a lubricant was applied (SuperLube, multipurpose synthetic grease, Part No. 21014). The chronoamperometry scans were conducted with the sensors orientated in the 0° direction and were tested consecutively starting with the 20 cm length pipe, followed by the 30 cm and finally the 40 cm length pipe. The sensor was then orientated 90° and tested again in the same manner.

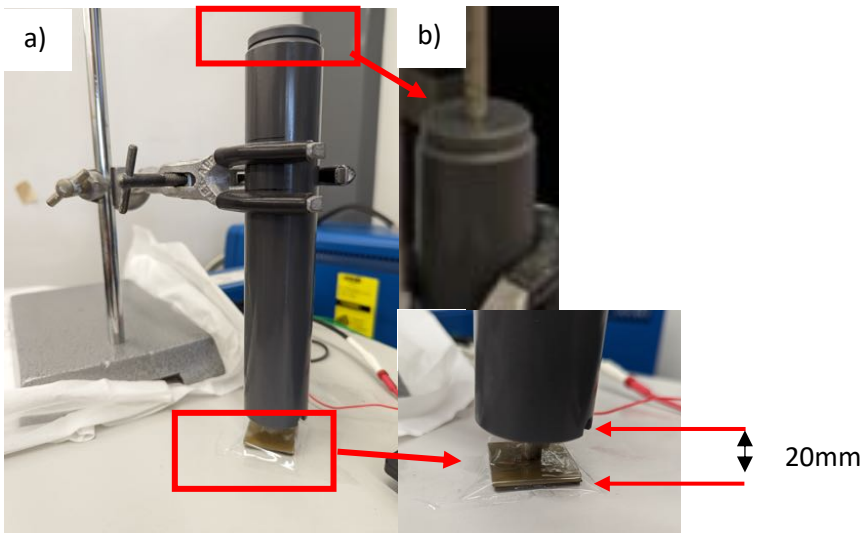

Figure C.1 a) PVC cylinder mounted 10mm over the PCB board, b) top of the PVC cylinder showing cut out where lubricated steel tube is marked and held another 10mm above where it is marked corresponding to a drop of 20mm, c) showing where impact occurs in the centre of the PCB board.

The data from the chronoamperometry scans is shown in Figure C.2. Each spike corresponds to the impact of the pipe hitting the PCB board.

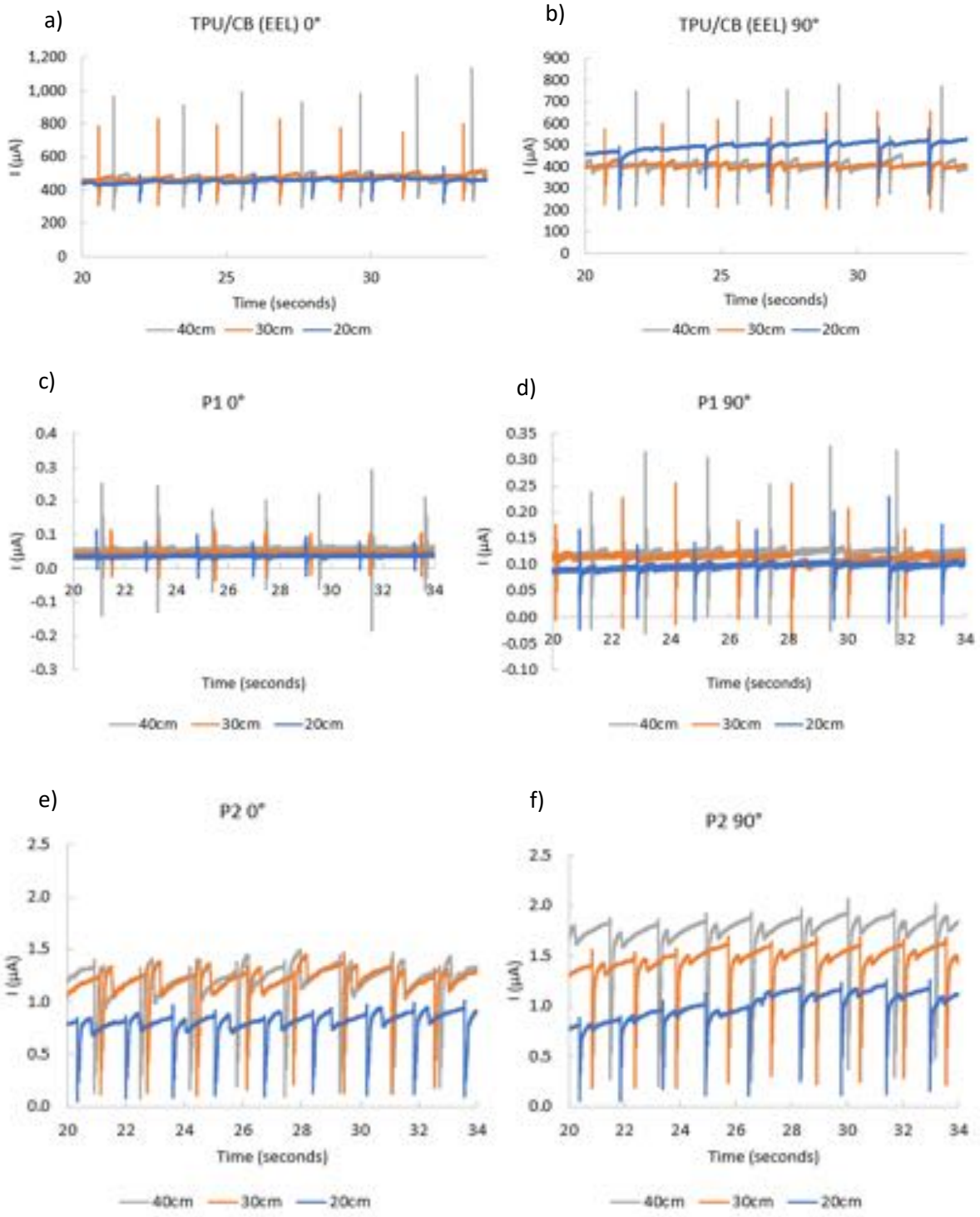
a)
TPU/CB (EEL) 0°
I (μA)
Time (seconds)
40cm
30cm
20cm
b)
TPU/CB (EEL) 90°
I (μA)
Time (seconds)
40cm
30cm
20cm
c)
P1 0°
I (μA)
Time (seconds)
40cm
30cm
20cm
d)
P1 90°
I (μA)
Time (seconds)
40cm
30cm
20cm
e)
P2 0°
I (μA)
Time (seconds)
40cm
30cm
20cm
f)
P2 90°
I (μA)
Time (seconds)
40cm
30cm
20cm

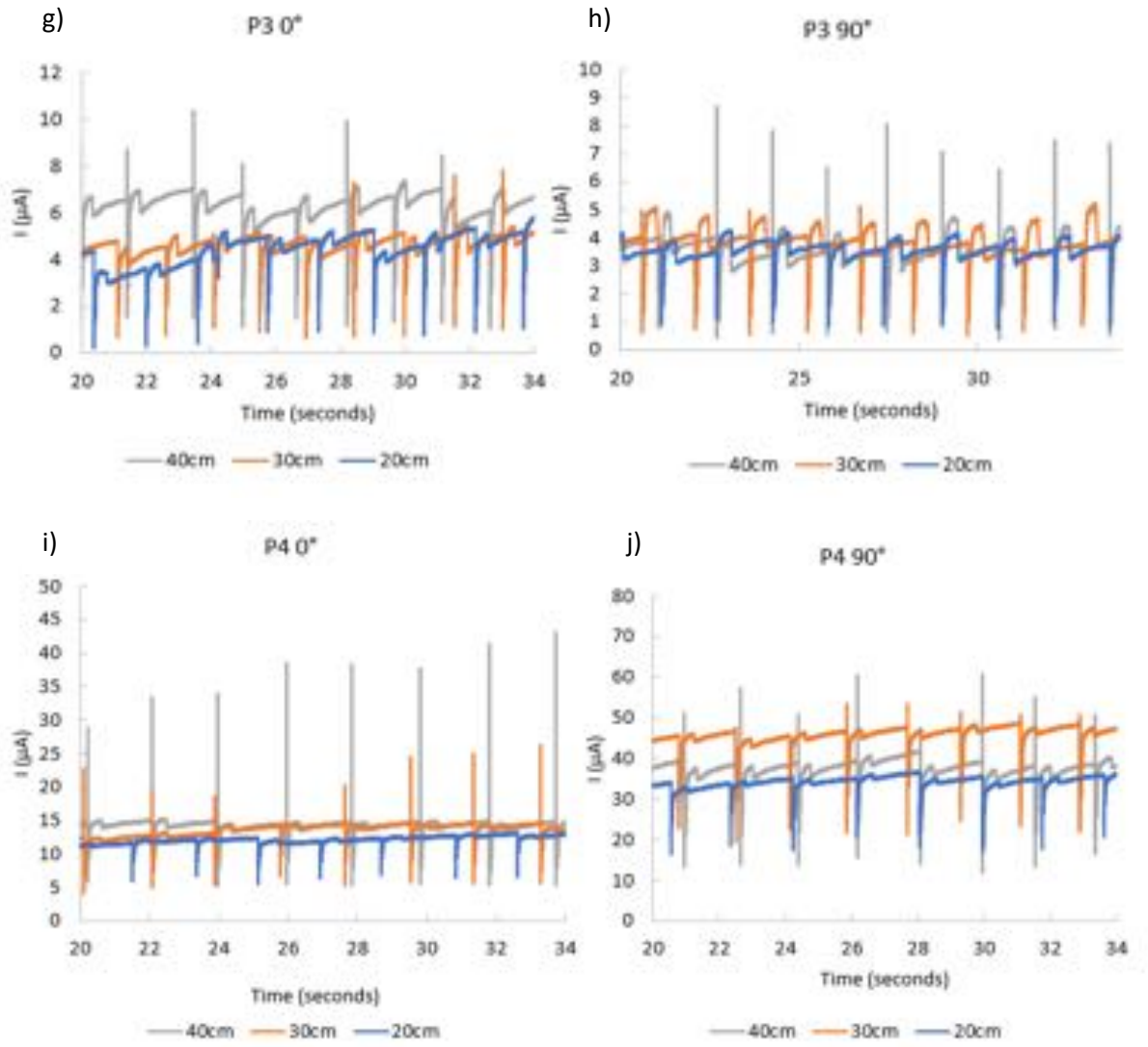

Figure C.2 Chronoamperometry scans showing impacts for 20, 30 and 40cm pipes for all sensors in 0° orientation (a, c, e, g, i) and 90° orientation (b, d, f, h, j)

The impact force is calculated using equation S1:

$$F = \frac{m*v}{2*t} \quad \text{(S1)}$$

Where *m* is the mass of the body (pipe), *v* is the velocity of the body, *t* is the time taken for the pipe to drop onto the PCB board.

The velocity the steel pipe travels before impacting to the PCB board (*v*) is calculated with equation S2.

$$v = \sqrt{u^2 + 2 * a * s} \quad \text{(S2)}$$

Where *v* is the final velocity, u is the initial velocity (here, u = 0 m/s), *a* is the acceleration due to gravity (9.8m/s^2) and *s* is the displacement (20 mm). The final velocity before impacting the PCB board is calcuated to be 0.62 6m/s. To find the time taken for the drop to occur (*t*), the calculated final velocity (v = 0.626m/s) and distance between the PCB board and lifted steel tube (d = 20mm) is entered into equation S3.

$$t = \frac{d}{v} \quad \text{(S3)}$$

The time taken for the steel pipe to drop is calculated to 0.0319 s. The *t* and *v* values are inserted in equation S1 with the mass of the steel pipes to find the calcuated impact force *F* in Newtons in Table C.1.

Table C.1 Calculated impact forces of the steel pipes onto the PCB board during the chronoamperometry scans

Pipe length (cm)	**20**	**30**	**40**
m (kg)	0.0316	0.0473	0.0636
F (N)	0.310	0.464	0.623

Appendix D - Effect of increasing milling time on $BaTiO_3$

SEM images of barium titanate powder as received (Figure D.1) after different milling times of 2 minutes (Figure D.2), 10 minutes (Figure D.3), 20 minutes (Figure D.4) and 30 minutes (Figure D.5) are shown below. It is apparent that, with increasing milling time, the $BaTiO_3$ particles become increasingly irregular and smaller in diameter. It is also apparent that the size of the original powder, marketed as 100 nm, is in fact broadly distributed.

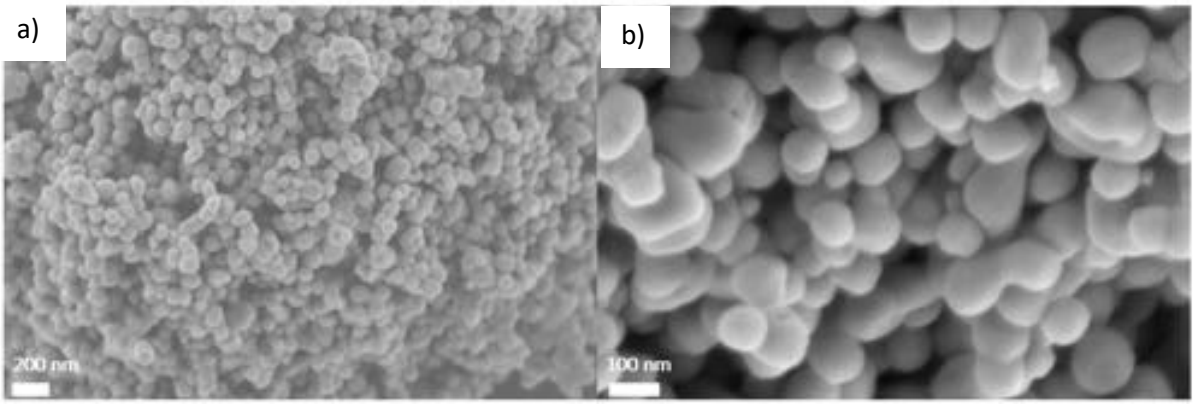

Figure D.1 Unmilled $BaTiO_3$ powder as seen at a) low and b) high magnification.

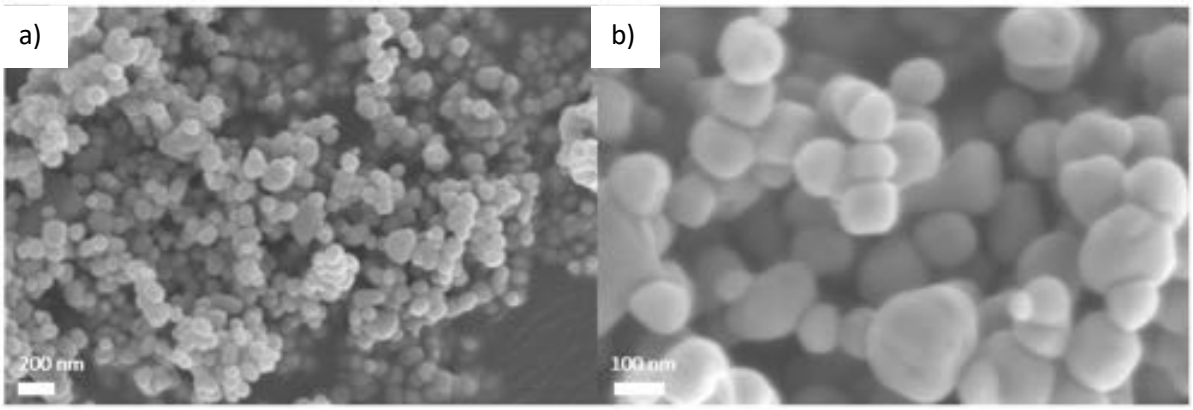

Figure D.2 $BaTiO_3$ milled for 2 min as seen at a) low and b) high magnification.

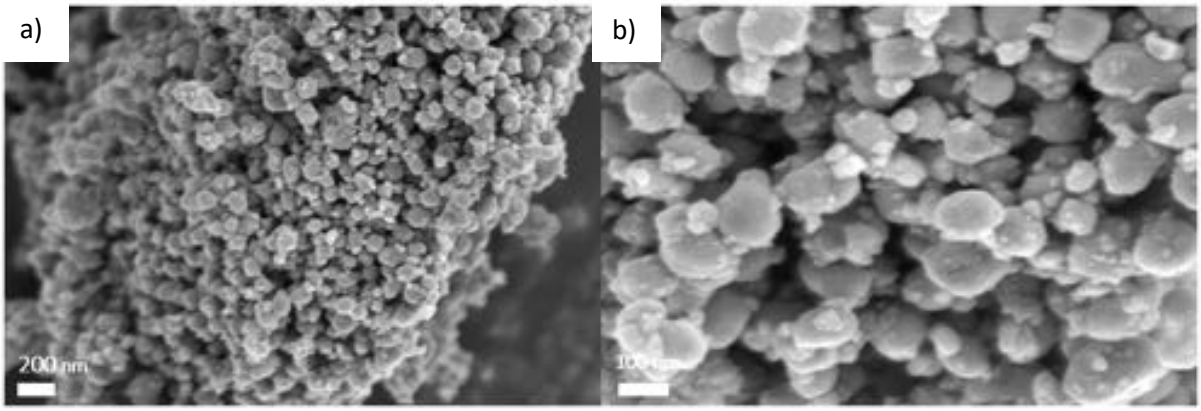

Figure D.3 $BaTiO_3$ milled for 10 min as seen at a) low and b) high magnification.

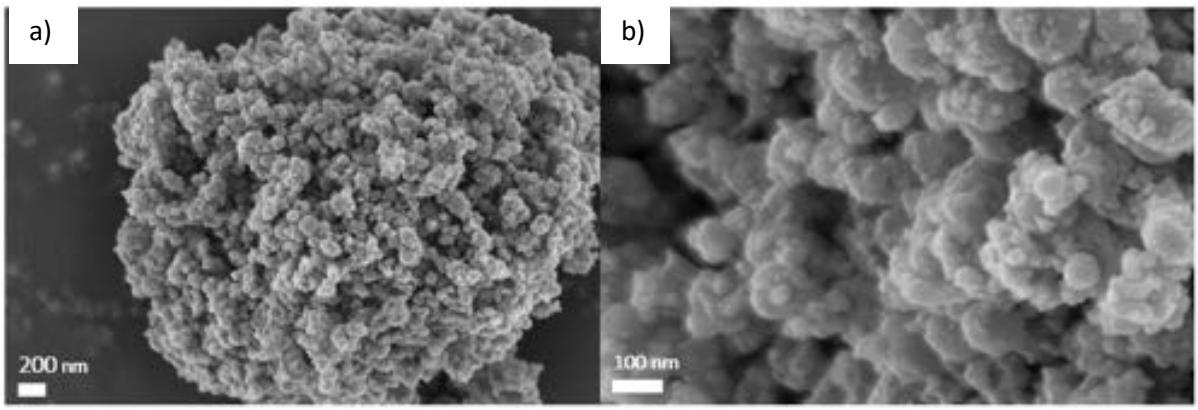

Figure D.4 $BaTiO_3$ milled for 20 min as seen at a) low and b) high magnification.

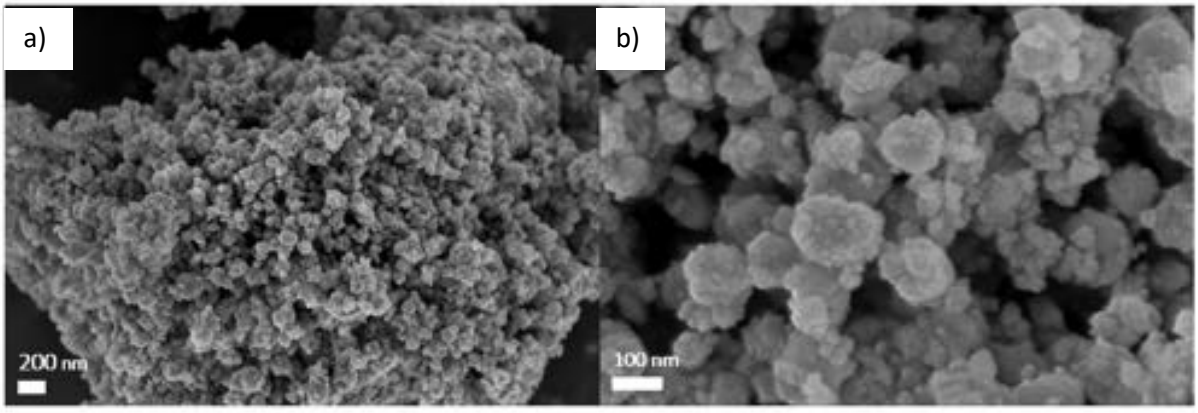

Figure D.5 $BaTiO_3$ milled for 30 min as seen at a) low and b) high magnification.

The resulting XRD scans from the milled powders are shown in Table D.1. Increasing the milling time reduces the $BaTiO_3$ crystallite size from an average of 85 nm to 26 nm. The standard deviation also decreases, indicating some improved homogeneity of the milled powder. In addition, the amount of BaCO3 (a natural by-product of $BaTiO_3$ powder production after sintering [1]) increases by 2 wt.% in the milled sample, likely due to the reaction of the powder within the ring mill, heating up and reacting with atmospheric carbon dioxide in the chamber.

Table D.1 XRD crystallite size values (in nm) and wt.% for the phases observed in the powdered samples, with errors.

Milled $BaTiO_3$ powder	$BaTiO_3$ crystallite size (nm)	$BaTiO_3$ wt.%	$BaCO_3$ wt.%
unmilled	85 ± 9	99 ± 2	2 ± 2
2 min	82 ± 8	98 ± 2	2 ± 2
10 min	40 ± 3	98 ± 2	2 ± 2
20 min	30 ± 2	97 ± 2	3 ± 2
30 min	26 ± 2	97 ± 2	4 ± 2

Appendix E - Effect of blending milled $BaTiO_3$ and TPPC into PVDF

The effect of incorporating various treatments (i.e., adding TPPC and milled $BaTiO_3$) into PVDF to create the 'piezoelectric' portion of the composite feedstock was investigated with XRD scans. Untreated PVDF was considered as term of comparison. As shown in Table E.1, scans on the PVDF filaments show that the amount of α phase in PVDF was found to reduce with the incorporation of $BaTiO_3$ powder in any form. In the contribution by Abdolmaleki and Agarwala, it was found that $BaTiO_3$ effectively reduced the proportion of the α phase and acted as a nucleation site for the β phase [2]. Through the XRD analysis, no β phase crystals were found when PVDF was blended with neat and unmilled $BaTiO_3$, but this may be due to the interference between the α and β phases that both have a peak at 20.8° [3]. The combination of TPPC and unmilled $BaTiO_3$ reduced the crystallite size of the α phase by 5 nm and favoured the growth of a sensible amount of β phase with an average crystallite size of 17 nm. Furthermore, the incorporation of milled $BaTiO_3$, (having reduced particle size and increased surface area) reduced the crystallite size of α phase to 13 nm. The crystallite size of the α phase reduced further with the combined addition of TPPC and milled $BaTiO_3$, which led to the smallest α crystallites.

Table E.1 Average crystallite size of the phases observed in the diffractograms of the filaments.

	α – PVDF (nm)	β – PVDF (nm)	Cubic $BaTiO_3$ crystallite size (nm)
PVDF	18 ± 2	-	
PVDF/$BaTiO_3$	15 ± 2	-	47 ± 8
PVDF/$BaTiO_3$ + TPPC	10 ± 1	17 ± 6	57 ± 7
PVDF/ milled $BaTiO_3$	13 ± 3	20 ± 10	23 ± 2
PVDF/ milled $BaTiO_3$ + TPPC	7 ± 1	20 ± 10	24 ± 2

Appendix F – Fracture surfaces and EDS maps of printed sensors

The printed sensors were immersed in liquid nitrogen, and then fractured to expose the inner printed infill. The fracture surface was analysed by scanning electron microscopy (SEM) and energy-dispersive X-ray spectroscopy (EDS). A low magnification image of the fracture surface of each sensor type is shown in Figure F.1a, F.2a, F.3a and F.4a. A higher magnification image of the fracture surface is shown in Figure F.1b, F.2b, F.3b and F.4b. All fracture surfaces appear to have a rough texture likely due to the dissimilarity of the two polymers TPU and PVDF fracturing under liquid nitrogen.

The corresponding EDS maps show no difference in carbon localisation between the fracture surfaces and the printed surfaces in Figure 11 (see article). The main difference is the localisation of $BaTiO_3$. $BaTiO_3$ particles are more clearly seen in the fracture surfaces, since they are not entirely encapsulated within the polymer matrix as they are in Figure 11. In particular, based on the EDS maps showing the distribution of barium, the localization of $BaTiO_3$ particles slightly differs between P1/P2 (Figure F.1c/F.2c) and P3/P4 (Figure F.3c/F.4c), as $BaTiO_3$ has a stronger tendency to agglomerate in P3 and P4 indicating that milling encourages this behaviour. However, in all cases, $BaTiO_3$ still appears to be evenly distributed throughout both polymers (TPU and PVDF) in the matrix.

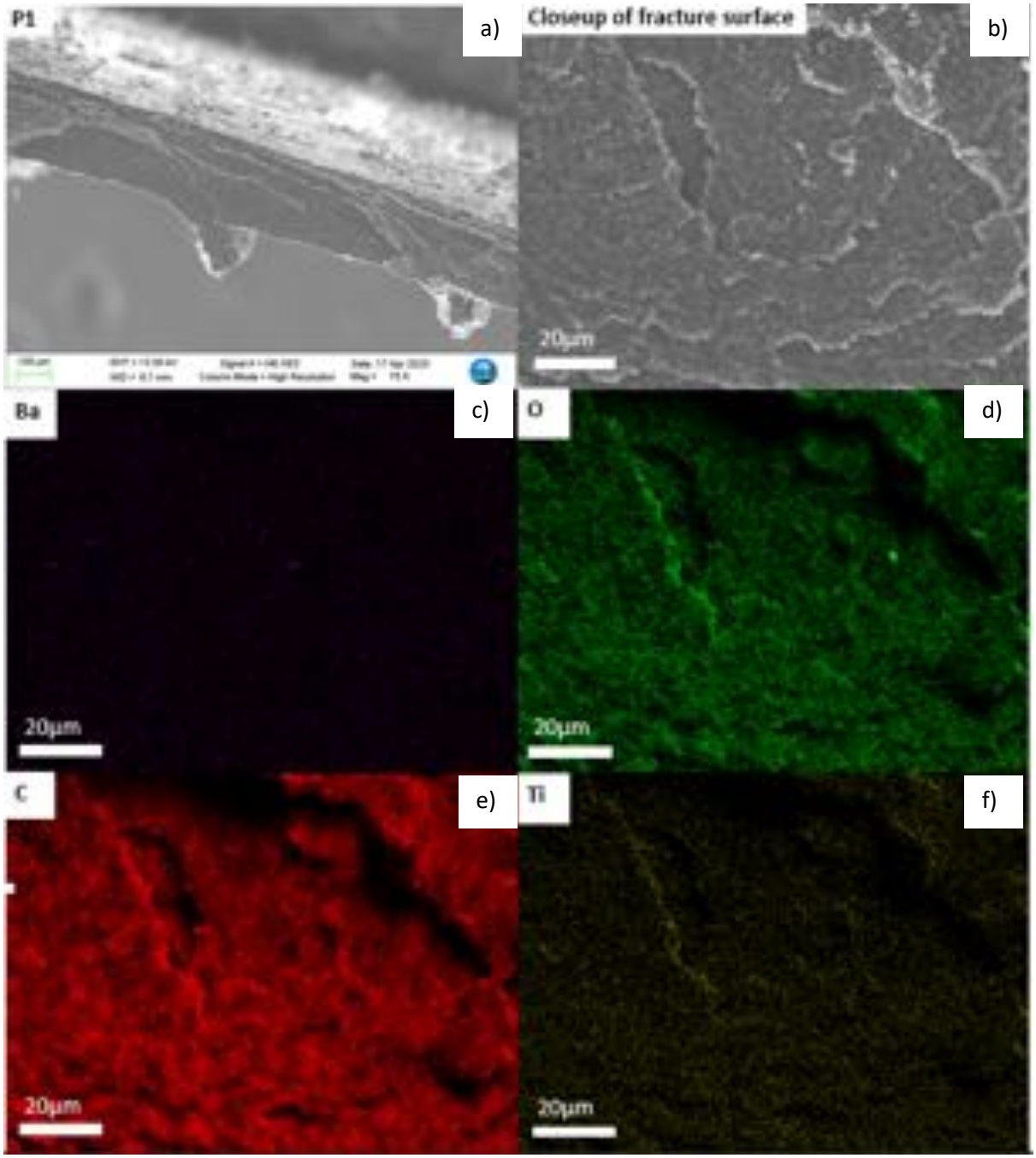

Figure F.1 SEM micrographs of the fracture surface of the P1 printed sensor under low a) and high b) magnification. EDS maps showing the localization of barium €, oxygen (d), carb€(e) and titanium (f).

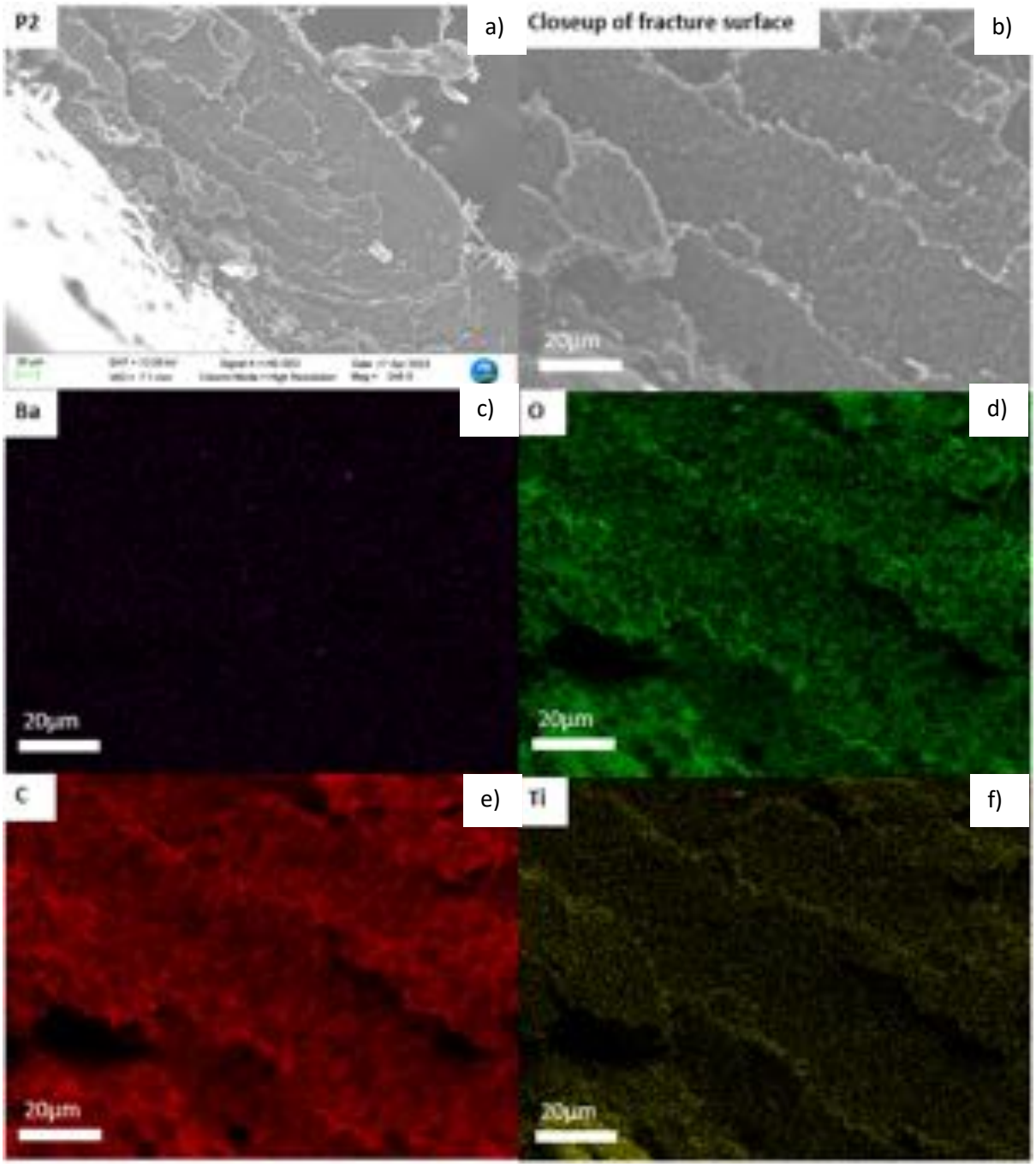

Figure F.2 SEM micrographs of the fracture surface of the P2 printed sensor under low a) and high b) magnification. EDS maps showing the localization of barium (c), oxygen (d), carbon (e) and titanium (f).

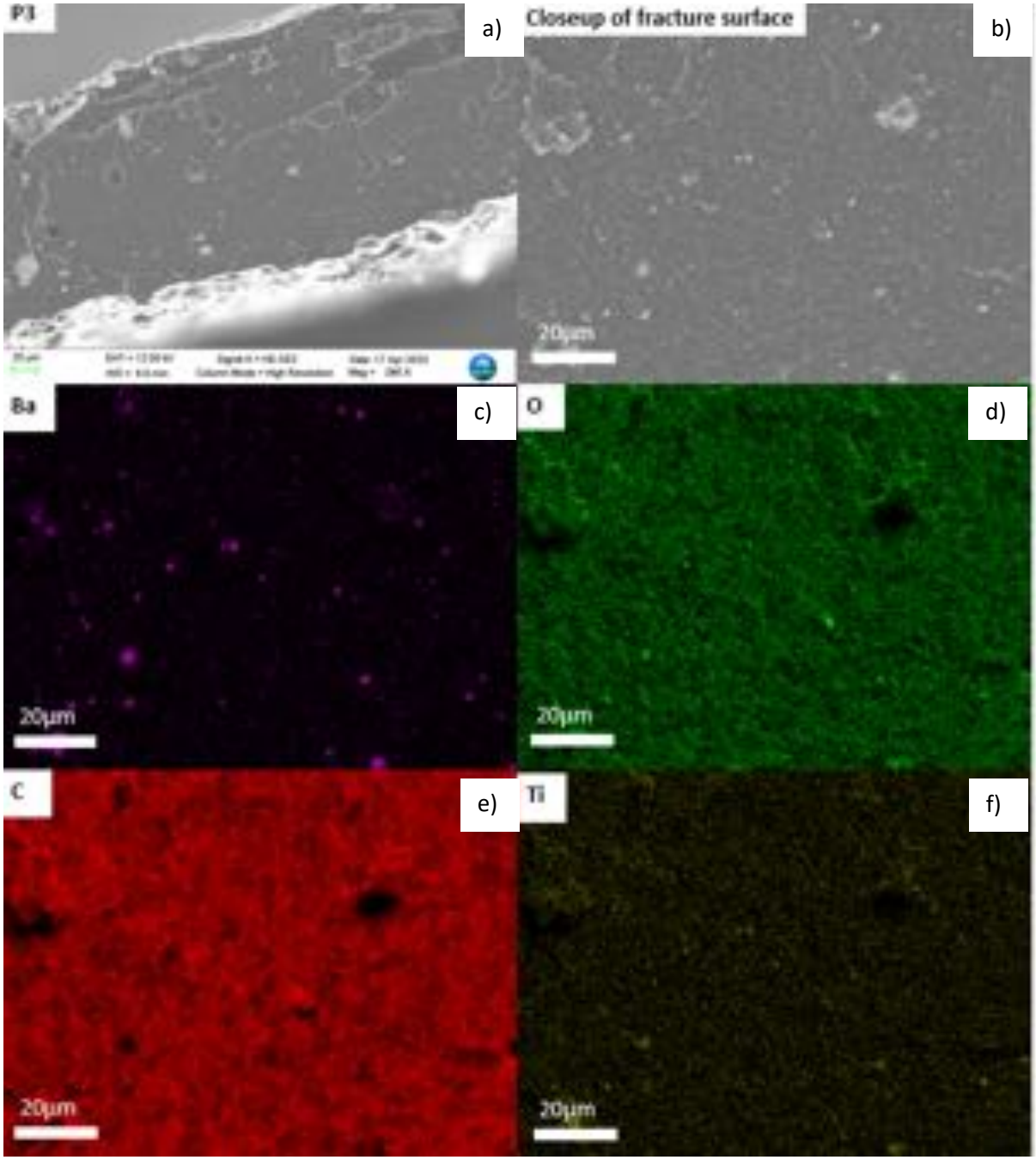

Figure F.3 SEM micrographs of the fracture surface of the P3 printed sensor under low a) and high b) magnification. EDS maps showing the localization of barium (c), oxygen (d), carbon (e) and titanium (f).

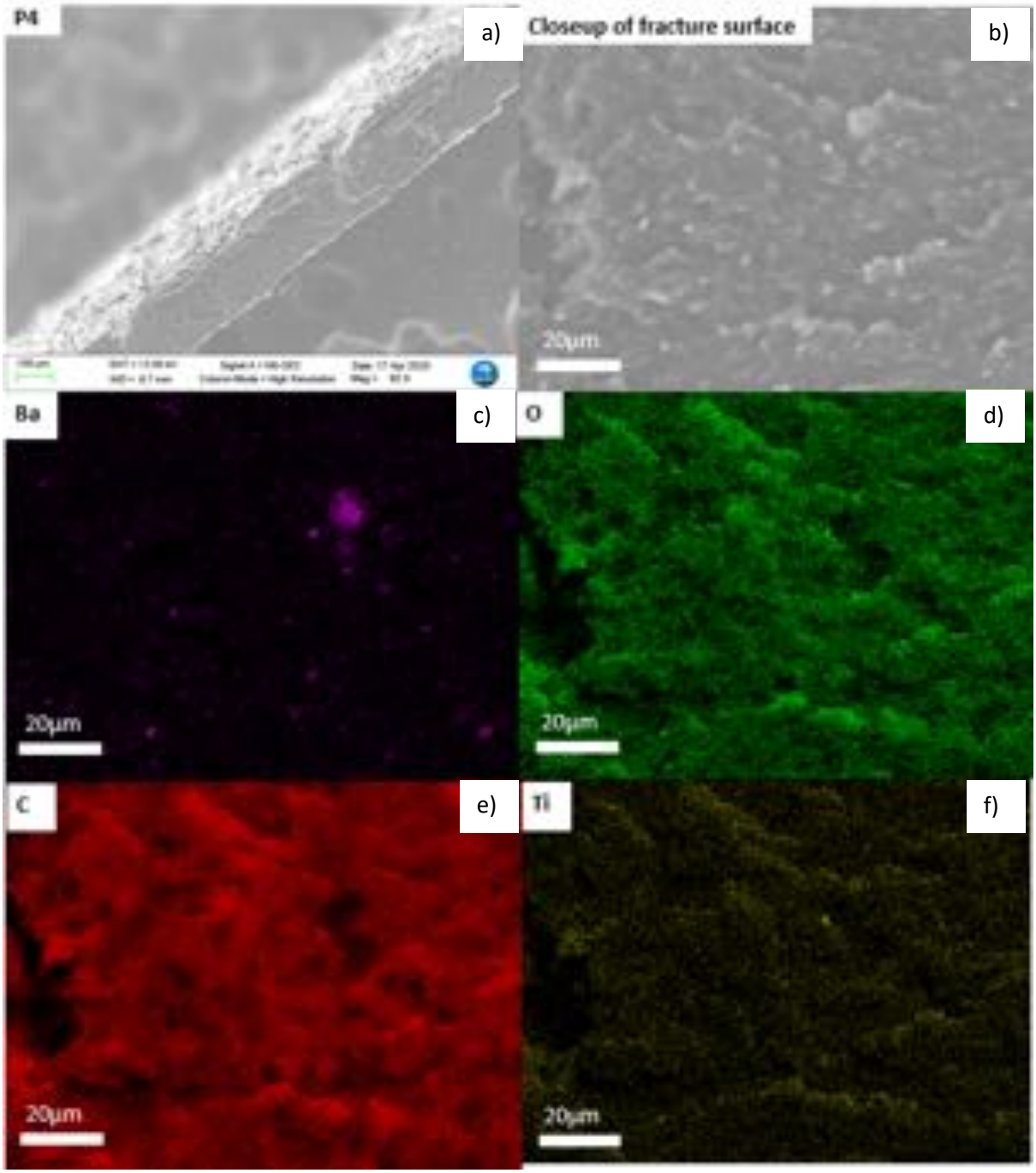

Figure F.4 SEM micrographs of the fracture surface of the P4 printed sensor under low a) and high b) magnification. EDS maps showing the localization of barium (c), oxygen (d), carbon (e) and titanium (f).

References

[1] A. Moghtada, A. Heidary Moghadam, R. Ashiri, Tetragonality enhancement in $BaTiO_3$ by mechanical activation of the starting $BaCO_3$ and TiO_2 powders: Characterization of the contribution of the mechanical activation and postmilling calcination phenomena, Int J Appl Ceram Technol. 15 (2018) 1518–1531. https://doi.org/10.1111/ijac.13019.

[2] H. Abdolmaleki, S. Agarwala, PVDF-$BaTiO_3$ nanocomposite inkjet inks with enhanced β-phase crystallinity for printed electronics, Polymers (Basel). 12 (2020) 1–12. https://doi.org/10.3390/polym12102430.

[3] R. Gregorio, Determination of the α, β, and γ crystalline phases of poly(vinylidene fluoride) films prepared at different conditions, J Appl Polym Sci. 100 (2006) 3272–3279. https://doi.org/10.1002/app.23137.